Title

Systematic feasibility analysis of a quantitative elasticity estimation for breast anatomy using supine/prone patient postures

Permalink

https://escholarship.org/uc/item/7nm3v909

Journal

Medical Physics, 43(3)

ISSN

0094-2405

Authors

Hasse, Katelyn
Neylon, John
Sheng, Ke
et al.

Publication Date

2016-03-01

DOI

10.1118/1.4941745

Peer reviewed

Systematic feasibility analysis of a quantitative elasticity estimation for breast anatomy using supine/prone patient postures

Katelyn Hasse,[a] John Neylon,[b] Ke Sheng,[c] and Anand P. Santhanam[d]
Department of Radiation Oncology, University of California, Los Angeles, Los Angeles, California 90095

Purpose: Breast elastography is a critical tool for improving the targeted radiotherapy treatment of breast tumors. Current breast radiotherapy imaging protocols only involve prone and supine CT scans. There is a lack of knowledge on the quantitative accuracy with which breast elasticity can be systematically measured using only prone and supine CT datasets. The purpose of this paper is to describe a quantitative elasticity estimation technique for breast anatomy using only these supine/prone patient postures. Using biomechanical, high-resolution breast geometry obtained from CT scans, a systematic assessment was performed in order to determine the feasibility of this methodology for clinically relevant elasticity distributions.

Methods: A model-guided inverse analysis approach is presented in this paper. A graphics processing unit (GPU)-based linear elastic biomechanical model was employed as a forward model for the inverse analysis with the breast geometry in a prone position. The elasticity estimation was performed using a gradient-based iterative optimization scheme and a fast-simulated annealing (FSA) algorithm. Numerical studies were conducted to systematically analyze the feasibility of elasticity estimation. For simulating gravity-induced breast deformation, the breast geometry was anchored at its base, resembling the chest-wall/breast tissue interface. Ground-truth elasticity distributions were assigned to the model, representing tumor presence within breast tissue. Model geometry resolution was varied to estimate its influence on convergence of the system. *A priori* information was approximated and utilized to record the effect on time and accuracy of convergence. The role of the FSA process was also recorded. A novel error metric that combined elasticity and displacement error was used to quantify the systematic feasibility study. For the authors' purposes, convergence was set to be obtained when each voxel of tissue was within 1 mm of ground-truth deformation.

Results: The authors' analyses showed that a ∼97% model convergence was systematically observed with no-*a priori* information. Varying the model geometry resolution showed no significant accuracy improvements. The GPU-based forward model enabled the inverse analysis to be completed within 10–70 min. Using *a priori* information about the underlying anatomy, the computation time decreased by as much as 50%, while accuracy improved from 96.81% to 98.26%. The use of FSA was observed to allow the iterative estimation methodology to converge more precisely.

Conclusions: By utilizing a forward iterative approach to solve the inverse elasticity problem, this work indicates the feasibility and potential of the fast reconstruction of breast tissue elasticity using supine/prone patient postures. © *2016 American Association of Physicists in Medicine.*
[http://dx.doi.org/10.1118/1.4941745]

1. INTRODUCTION

Breast cancer is the most commonly diagnosed cancer for women in the United States, with about one in eight U.S. women developing invasive breast cancer over the course of her lifetime.[1] The general approach to early stage breast cancer treatment usually involves a lumpectomy, followed by postoperative radiotherapy, which significantly reduces the risk of cancer recurrence. Postoperative breast radiotherapy can be challenging because of the deformable nature of the breast tissue. Day-to-day changes in breast anatomy and positioning present an obstacle when trying to attain an ideal and repeatable patient setup. It has been previously documented that the breast alignment can vary by more than 5 mm in any dimension from one day to another without the use of immobilization devices.[2] Existing immobilization devices designed for rigid anatomies are not suitable for fixing the breast position. Engineering novel immobilization devices for precise and reproducible breast setup require modeling of the breast deformation for given forces applied to the breast surface.[3] Therefore, the first step in engineering such immobilization devices is a systematic development of subject-specific biomechanical breast models.

High-resolution biomechanical physics-based models have been used to develop patient-specific representations of deforming anatomy.[4] Sophisticated biomechanical models can

simulate deformations and physiological changes in different anatomies, creating a dynamic physical atlas.[5] It is necessary that these models be patient-specific in order to use material properties of soft tissue to correctly predict outcomes and response to radiation therapy, calculate mechanical deformation of surrounding tissue caused by tumor growth, and accurately model tissue movement during radiation therapy treatments.[6–8] Biomechanical models of the breast have also been used to more precisely locate cancerous tissue and simulate breast shape during a variety of clinical applications.[2] Biomechanical models must take into consideration the laws governing the mechanical properties of tissue—elastography is a noninvasive way to image the physical distribution of these properties.[9] Elastography techniques focus on mapping the elastic properties of soft tissue into a spatial distribution and have previously been used for modeling anatomic sites such as the breast and prostate.[10] Knowing the distribution of elastic properties throughout soft tissue can lead to design and development of immobilization devices in addition to yielding valuable biomechanical information in a patient-specific manner.

Elastography imaging techniques have been previously investigated by peers for differentiating benign from malignant disease, possibly reducing the overall number of breast biopsies.[11–13] These methods generally assess tissue and lesion stiffness by perturbing the tissue, measuring the internal tissue displacements, and inferring a spatial distribution of mechanical properties from the measured mechanical response.[14–16] Popular elastography imaging techniques include shear wave elastography, where the speed of a shear wave throughout tissue provides a quantitative measure of lesion stiffness, and freehand elastography, where a handheld transducer is used to axially compress the tissue a few millimeters.[17] Both ultrasound- and MR-based implementations of these techniques have been shown as feasible ways to identify and characterize cancerous tumors in soft tissues, as malignant lesions exhibit considerably higher elasticity than the surrounding parenchymal tissue.[11,18,19]

A critical limitation in performing breast elastography within a radiotherapy setting is that the clinical breast radiotherapy protocols only involve prone and supine CT scans.[20] With additional MR and ultrasound imaging being unattainable within a clinical radiotherapy workflow, it is important to study the feasibility and accuracy of deriving breast tissue mechanical properties based on the two CT scans.

The focus of this paper is to formulate a methodology for performing breast elastography with subject-specific clinical supine/prone CT data, and to systematically validate and quantify the accuracy of this methodology. A linear elastic biomechanical model, which has been previously used for representing head and neck deformations,[5] will be employed as a deformation model to represent the breast anatomy. Each mass element of the model denotes a single voxel from the supine or prone CT image data. The underlying elasticity is then estimated using a gradient descent binary search algorithm coupled with a fast-simulated annealing (FSA) based model parameter optimization.

2. MATERIALS AND METHODS

The primary aim of this study was to formulate a method to estimate the Young's moduli (YM) associated with each voxel in the breast anatomy and to quantitatively assess the accuracy of the estimated values using virtual breast phantoms. From a mathematical perspective, reconstructing the elasticity distribution of tissue can be approached in either a direct or an inverse manner. The direct approach reconstructs an elastographic image by converting the strain value at each voxel to a relative Young's modulus using a simple model constraint, such as Hooke's law.[21] This approach is limited, however, and has been shown to be inferior when compared to the inverse approach.[22] The inverse approach, or model-based method, is an iterative approach that allows for more reasonable and realistic model constraints. Peers have formulated the inverse elasticity problem as a parameter optimization problem with an objective to minimize the difference between measured displacement and that computed by a biomechanical model representing observed mechanical behavior.[19]

In our approach, we formulated breast elastography as an inverse problem. The supine-to-prone breast deformation is known to be gravity-induced.[23,24] We used the observed tissue displacement between supine/prone postures as our measured ground-truth displacement. A biomechanical simulation was employed as the forward deformation model to evaluate the inverse breast elasticity problem, with its parameters being iteratively updated. It has been shown in Ref. 5 that the deformation of the biomechanical model acted upon by gravity matches the expected soft-tissue response, indicating its potential for modeling the supine-to-prone breast deformation. Implementation of this model in a graphics processing unit (GPU) environment allowed for fast and accurate breast tissue elasticity estimations.

In this section, we first present the GPU-based forward deformation model that was devised to represent the breast anatomy. We then present the inverse formulation that was used to estimate the breast tissue elasticity. Finally, we present our experiments in systematically assessing the accuracy of the estimated tissue elasticity.

2.A. Forward problem

While the forward problem is previously discussed in Ref. 5, for clarity, we hereby present the model.

2.A.1. Model initialization and geometry

The biomechanical model was constructed from clinically acquired or virtually constructed CT data. We defined deformation space as the virtual space where the model geometry can be instantiated and deformed. The model geometry was represented by mass elements corresponding to the center of each voxel of anatomy in the CT image. Mass elements were connected by mass-spring damping (MSD) connections in the deformation space. Connecting the mass elements with each other using a spring damper formulation ensured that the mass

elements could deform in a physically realistic manner. The connections were established as follows: A local neighborhood search was performed in a parallelized manner around each mass element to find nearby elements. When a nearby element was within a threshold distance (determined by the voxel size of the input CT, approximately 3 mm in our case) from the search element, a MSD connection was established and the nearby element became a connected element for the given search element. The rest length and orientation of each connection were then recorded and assigned a Young's modulus and a Poisson's ratio as the final step in the model initialization.

2.A.2. Forward deformation computation

The corrective forces on each mass element were calculated as a summation of tensile force, shear force, and a dashpot damping force. At rest state, the elastic internal corrective forces were set to zero. When deformed, the model's mass elements were relocated to new positions inside the deformation space, which caused the internal corrective forces to be nonzero. For each mass element, a, the tensile force, $\vec{f}_{Y,ab}$, shear force, $\vec{f}_{S,ab}$, and the dashpot damping force, $\vec{f}_{v,ab}$, were calculated for each connected element, b, and summed to find internal corrective force, $\vec{f}_a$,

$$\vec{f}_a = \sum_b \left(\vec{f}_{Y,b} + \vec{f}_{S,b} + \vec{f}_{v,b} \right). \tag{1}$$

Once the internal forces were computed, the new positions, $\vec{x}_a^{n+1}$, and velocities, $\vec{v}_a^{n+1}$, of the mass elements were updated from the values $(\vec{x}_a^n, \vec{v}_a^n)$ at the previous iteration n, using implicit (backward) Euler integration,

$$\vec{v}_a^{n+1} = \vec{v}_a^n + \left(\frac{\vec{f}_a}{m_a} + \vec{g} \right) \delta, \tag{2}$$

$$\vec{x}_a^{n+1} = \vec{x}_a^n + \vec{v}_a^{n+1} \delta, \tag{3}$$

where δ was the time step between iterations, m_a was the mass of mass element a, and $\vec{g}$ was the acceleration due to gravity.

The Euclidean distance between $\vec{x}_a^n$ and $\vec{x}_a^{n+1}$ for each mass element was taken to be the ground-truth displacement for that mass element, and then the biomechanical model was reset with an initial guess elastic distribution. The iterative binary search optimization scheme was utilized until convergence occurred. The initial guess distributions and iterative binary search optimization schemes are further discussed in Secs. 2.B and 2.C.

2.B. Inverse analysis

Solving the inverse elasticity problem was accomplished by iteratively deforming the model from rest state, as described in Sec. 2.A.2. A gradient-based binary search (further discussed in Sec. 2.B.1) was used as an iterative optimization scheme to update the spatial-elastic distribution in order to minimize the discrepancy between ground-truth and computed mechanical response, or displacement, for each voxel, while

a fast-simulated annealing algorithm was simultaneously employed to optimize model parameters (further discussed in Sec. 2.C.4).

2.B.1. Iterative elasticity estimation

The iterative scheme for recovering the Young's modulus distribution was derived from the relationship between Young's modulus and displacement.[25] An elastic solid can be viewed as a series of mass elements connected by a grid of ideal linear elastic connections, where the elastic modulus acts on each mass element similarly to a material constant. Likewise, the resulting displacement can be related to the stiffness of the material,

$$F_E[i] = E[i] \frac{\Delta L[i]}{L[i]}, \tag{4}$$

where F_E is the elastic force upon mass element i, E is the elastic modulus, ΔL is the change in length of the connections connected to mass element i, and L is the initial length of the connections for mass element i. This equation illustrates that the elastic modulus and displacement are inversely related—if elastic modulus increases then displacement must decrease and vice versa. This principle defines the reasoning behind the iterative process for estimating elasticity.

The general basis of our reconstruction technique is to minimize the difference between the ground-truth and calculated displacements. Given an initial Young's modulus, the biomechanical model will provide theoretical estimates of mass element displacements. These displacements are then compared with the ground-truth displacement vectors and Young's modulus is iteratively updated until convergence is achieved. Intermittent mass element displacement values are generated on a per voxel basis by updating the Young's modulus (E) values as follows:

(a) Initialize values of $E[i]$, $E_{\min}[i]$, and $E_{\max}[i]$.
(b) Compute the displacement residual vector $\Delta d[i]$ by subtracting the calculated displacements from the ground-truth displacement at each voxel.
(c) Update $E_{\min}[i]$ and $E_{\max}[i]$:
   (i) If $\Delta d[i] > 0$, $E_{\min}[i] = E[i]$ and $E_{\max}[i] = E_{\max}[i]$,
   (ii) If $\Delta d[i] < 0$, $E_{\min}[i] = E_{\min}[i]$ and $E_{\max}[i] = E[i]$.
(d) Estimate next values of E using $E[i+1] = (E_{\min}[i] + E_{\max}[i])/2$.
(e) Repeat steps (b)–(d) until a suitable stopping criterion has been reached.

This iterative procedure is based upon the modified Gauss–Newton method,[26,27] which was chosen because it requires no assumption about the homogeneity of the tissue in question, the implementation is straightforward, and the convergence occurs within $O(\log n)$ iterations. For our purposes, the range of Young's modulus values is given by $E_{\min}[i] < E[i] < E_{\max}[i]$, where $E_{\min}[i]$ and $E_{\max}[i]$ are typically 1 and 200 kPa for living soft tissues.[27,28] Convergence was obtained when each voxel of tissue was within 1 mm of the ground-truth deformation.
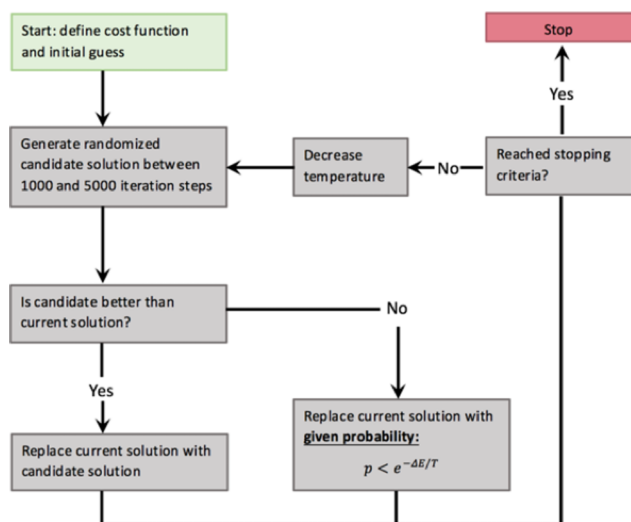
FIG. 1. Flow chart depicting fast-simulated annealing process.

2.B.2. Fast-simulated annealing

Besides elasticity, another parameter of the biomechanical model that needs to be optimized is the number of iterations for the biomechanical model. Iteration number refers to the deformation time for each iteration of the simulation. This is important because deformation time greatly impacts whether the system reaches an equilibrium state or whether the system is still in transition when the displacement values are recorded.

FSA was chosen to optimize iteration number because even in the presence of noisy data, it may not find the optimum solution, but it will find a very good solution very quickly. The FSA algorithm generates randomized iteration number candidates and checks if this candidate solution is better than the current solution. If so, the current solution is replaced with the candidate solution, but if not, the current solution is replaced with a given probability. This allows us to accept iteration numbers that are not ideal in order to explore more of the possible solution space. The probability decreases with a logarithmic temperature scheme until the system converges or a set computation time has been exhausted. The lowered temperature limits the number of nonideal iteration numbers

that are accepted so that the solution is allowed to approach the global minimum. A flow chart describing the FSA process is shown in Fig. 1.

2.C. Numerical analysis

To enable a systematic study of the inverse analysis process, the biomechanical model was employed to generate a hemispherical geometry representing a breast in order to simulate the ground-truth displacement vectors. The hemispherical geometry was approximated from a volume rendered patient CT image of a breast in the prone position [Fig. 2(a)]. The chest-wall/breast tissue attachment interface is mimicked by anchoring the base of the hemisphere to prevent motion in the top layer of mass elements, which is illustrated in Fig. 2(b).

2.C.1. Virtual breast phantoms

Two different hemispherical geometries were constructed with 1 mm^3 voxels to represent different model resolutions. The lower resolution simulation contained 100 000 voxels and had a 64 voxel diameter, while the higher resolution model contained about 600 000 voxels with a 128 voxel diameter. A homogeneous elastic modulus distribution of 20 kPa was initially used to represent a mixture of fatty and glandular breast tissue.[22] Spherical inhomogeneities with diameters of 5, 10, and 15 mm were placed within the geometry.[29] These spherical masses, representing breast tumors within the tissue, were used to signify ductal carcinomas *in situ* (DCIS), invasive ductal carcinomas (IDC), and fibroadenomas, with elasticity values of 75, 90, and 110 kPa, respectively, as derived from the literature and shown in Table I.[30] The breast geometry was divided into quadrants and for each distribution, a tumor was placed either in the center of the hemisphere or the center of one of the quadrants. Combining the different types, sizes, and locations of tumors along with the different image resolutions resulted in 90 different ground-truth elasticity distributions. The biomechanical breast model was deformed in turn with each of these ground-truth elasticity distributions, with the resulting ground-truth displacements calculated as explained above.
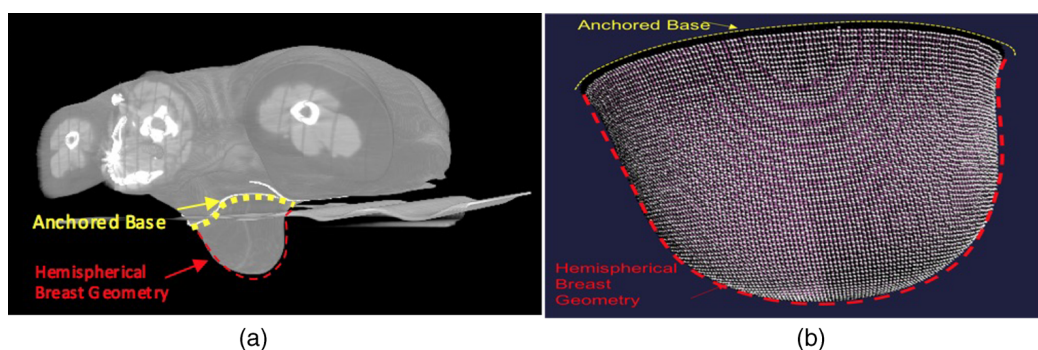

FIG. 2. Volume renderings of prone DICOM CT (a) and biomechanical simulation with anchored base of a 128-voxel diameter hemisphere to mimic chest-wall interface (b).

TABLE I. Elasticity values for different components of breast tissue found from the literature (Ref. 26).

Breast tissue type	Fatty/glandular tissue (kPa)	Fibrous tissue (kPa)	Ductal carcinoma *in situ* (kPa)	Invasive ductal carcinoma (kPa)
Tissue elastic modulus	20	110	75	90

2.C.2. Inverse analysis with no a priori information

After the ground-truth deformation was recorded, the estimated elasticity was reset to an initial guess elasticity distribution. Primarily, the elasticity was reset to a homogeneous initial guess in which no assumptions were made about the anatomy in question. This initial guess was used in order to investigate the robustness of our methodology by showing that the system could converge regardless of the disparity between the initial guess and the ground-truth elastic distribution. The time and accuracy of the convergence for each ground-truth distribution were recorded and analyzed.

2.C.3. Inverse analysis with a priori information

We then performed the same study using *a priori* information, which would be gained from the HU values obtained from the supine/prone CT images. For the purposes of our feasibility study, HU values were simulated and assigned to each voxel with values from the literature depending on whether the voxel represented normal fibroglandular tissue or was a part of one of our simulated spherical tumors.[31] These HU values were input into our simulation, and if the HU value for a voxel was above a certain threshold, that voxel was assigned a higher initial elastic modulus. It is expected that, using the *a priori* information, we can more precisely define the boundary of a tumor and decrease the computation time.

2.C.4. Fast-simulated annealing

A FSA algorithm is used to optimize iteration number while the binary search to optimize elasticity is performed simultaneously, which is illustrated in Fig. 3. To ascertain whether the fast-simulated annealing obtained an optimum

solution, displacements were recorded for a random sample of the ground-truth elasticity distributions, and then the simulation attempted to recreate the ground-truth elasticity distributions both with and without the FSA optimization. For scenarios, when the FSA algorithm was not employed, the iteration number was set to 4000, which was the ground-truth iteration number. The accuracy of the FSA algorithm is further explored in Sec. 3.C.

2.C.5. Error metric

The metric used for quantifying the accuracy of the inverse analysis was a combination of both the estimated elasticity and the displacement error produced using the estimated elasticity. Higher elasticity values of the tumor voxels represent stiffer connections, so a small error in the elastic moduli did not as greatly increase the displacement error when compared to the more elastic interactions with the normal tissue voxels. To determine whether or not our elasticity accuracy will translate to the required clinical accuracy, we deformed the synthetic phantoms and plotted the maximum displacement versus elasticity for hemispheres with different homogeneous elastic moduli distributions, and fit a curve to the plotted points, which is shown in Fig. 4. The resulting equation is

$$d \cong 16.11 - 0.231\,297 * E + 0.001\,122\,46 * E^2, \tag{5}$$

which fit the data with an R^2 value of 0.996. Using this equation, we concluded that a displacement differential of $\Delta 1$ mm (or submillimeter clinical accuracy) corresponds to an elasticity differential of $\Delta 0.5$ kPa for voxels with elastic moduli falling somewhere in the normal tissue range (around 15–25 kPa). Similarly, a displacement differential of
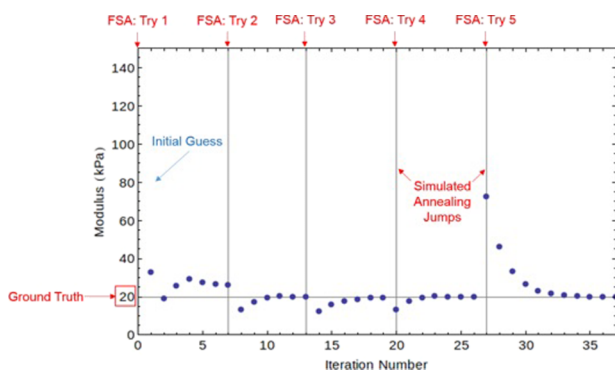

FIG. 3. Illustration of the simultaneous binary search and FSA algorithms. The red lines indicate that a FSA jump was performed, where the binary search process is illustrated by the points (see color online version).
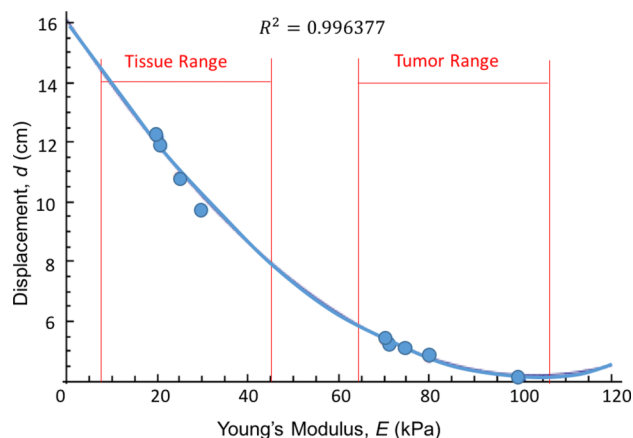

FIG. 4. Displacement versus Young's modulus fitted plot.

Δ1 mm corresponds to an elasticity differential of Δ3 kPa for voxels with higher elasticity values in the tumor range (around 70–100 kPa). The values of 0.5 and 3 kPa were approximated to 1 and 5 kPa for more robust binning and were used to bin the elasticity differentials between estimated and ground-truth elasticity distributions for the purposes of our study.

The results can then be given in terms of both elasticity accuracy and displacement accuracy. Elasticity error was derived by using a L1 norm (subtracting the resulting elasticity distribution from the ground-truth elasticity distribution), binning the elasticity error into 1 and 5 kPa bins, and calculating the percentage of mass elements that fell in each bin. We calculated displacement accuracy by subtracting the resultant displacement of each mass element from the ground-truth displacement, and focusing on the results with submillimeter accuracy. Other elastography estimation methods, such as combined ultrasound and FE models, strive for displacement error that is less than the smallest tumor diameter that can be found in breast tissue, which is around 3 mm.[32] For a direct comparison, the displacement accuracy that is less than 3 mm is also presented for individual cases in Sec. 3.

Besides looking at the results averaged over all of the distributions, we present the three other criteria that were also investigated: (a) relation between the use of *a priori* information and accuracy, (b) relation between the image resolution geometry and the accuracy, and (c) effectiveness of the FSA algorithm. A two-sample *t*-test was performed to analyze whether the statistical significance of the differences in the means of each population for each of the three criteria listed above. Volume renderings of the resultant and ground-truth elasticity distributions were also used to visually analyze the results as an addendum to the numerical results. The results gleaned from the systematic study are presented in Sec. 3.

3. RESULTS

In this section, we present the results obtained from the systematic study. To illustrate the aptitude of the forward model for representing gravity-induced soft-tissue deformations, the biomechanical simulation was used to establish geometry from a prone breast DICOM CT [(a) and (b)] with a homogeneous elasticity distribution. This geometry was then deformed with gravity to simulate the supine orientation [(c) and (d)], illustrating that the model can accurately represent the soft-tissue deformation between prone and supine breast postures. Figure 5 shows DICOM CT [(a) and (c)] and biomechanically simulated [(b) and (d)] prone and supine breast positions. Figure 5(e) shows an overlay of images (c) and (d). ImageJ was used to perform an image comparison and the images were shown to be 85.23% similar. The mismatch between the two images, highlighted in yellow, can be explained by segmentation errors, as the breast was manually segmented from the DICOM CT images, and intensity differences between the DICOM CT and the mass elements in the biomechanical simulation.

3.A. Model resolution

To analyze the impact of the breast model resolution on the estimated elasticity, the simulation was performed with two different resolutions of hemispheres, as mentioned in Sec. 2.C.1. The lower resolution, 64 voxel diameter hemisphere converged on average with 98.87% of the voxels within 1 mm of the ground-truth results. This corresponded to 92.02% of voxels being within 1 kPa of their ground-truth elasticity values, and 96.92% of voxels converging within a 5 kPa window. The higher resolution, 128 voxel diameter hemisphere converged on average with 96.19% of the voxels within 1 mm of the ground-truth displacement, resulting in 86.15% of voxels converging within a 1 kPa elasticity window and 98.38% converging within 5 kPa. These results are summarized in Table II. A two-sample *t*-test of 20 different images shows that the differences between the results of the lower and higher resolution datasets were not significant ($P > 0.05$). Though the average elasticity error for the 1 kPa bins in each instance seems to be dissimilar, the *t*-test considers a one-to-one correspondence between the values in the samples. For example, the elasticity error of every ground-truth elasticity distribution is compared between the lower and higher resolution cases.

Because a multitude of distributions were considered, the differences between the average values were not significant. This implies that regardless of image resolution, we can produce results with similar accuracy, which is paramount to implementation in the clinical setting. More specifically, Table III shows examples of the results of lower and higher resolution datasets for a large fibroid in the center, a small IDC in quadrant II, and a medium DCIS in quadrant IV. These results again illustrate that for multiple tumor locations, regardless of tumor type or size, both the low and high-resolution reconstructions produce similar elasticity distribution. Figure 6 shows volume renderings of a medium IDC located in quadrant II for both the low-resolution (a) and the high-resolution (b) hemispheres. Both cases are visually and numerically similar—the boundary between the differing elasticity values is well-differentiated for both low- and high-resolutions. The inverse elasticity algorithm is invariant to image resolution, further indicating that image resolution will not hinder the accuracy of our reconstruction.

3.B. *A priori* information

Two different initial guess distributions of elasticity values were investigated. The first required no *a priori* information about the underlying anatomy—the initial guess was set to a homogeneous elasticity value of 10 kPa. In the second case, *a priori* information was developed to be indicative of representative HU values that would come from the prone/supine CT scans taken in the clinic. Each ground-truth elasticity distribution was investigated starting with both types of initial guess. Table II shows the results averaged over every distribution both with and without the *a priori* initial guess. It can be seen that the *a priori* information increased the elasticity and displacement accuracy overall. Table IV shows a
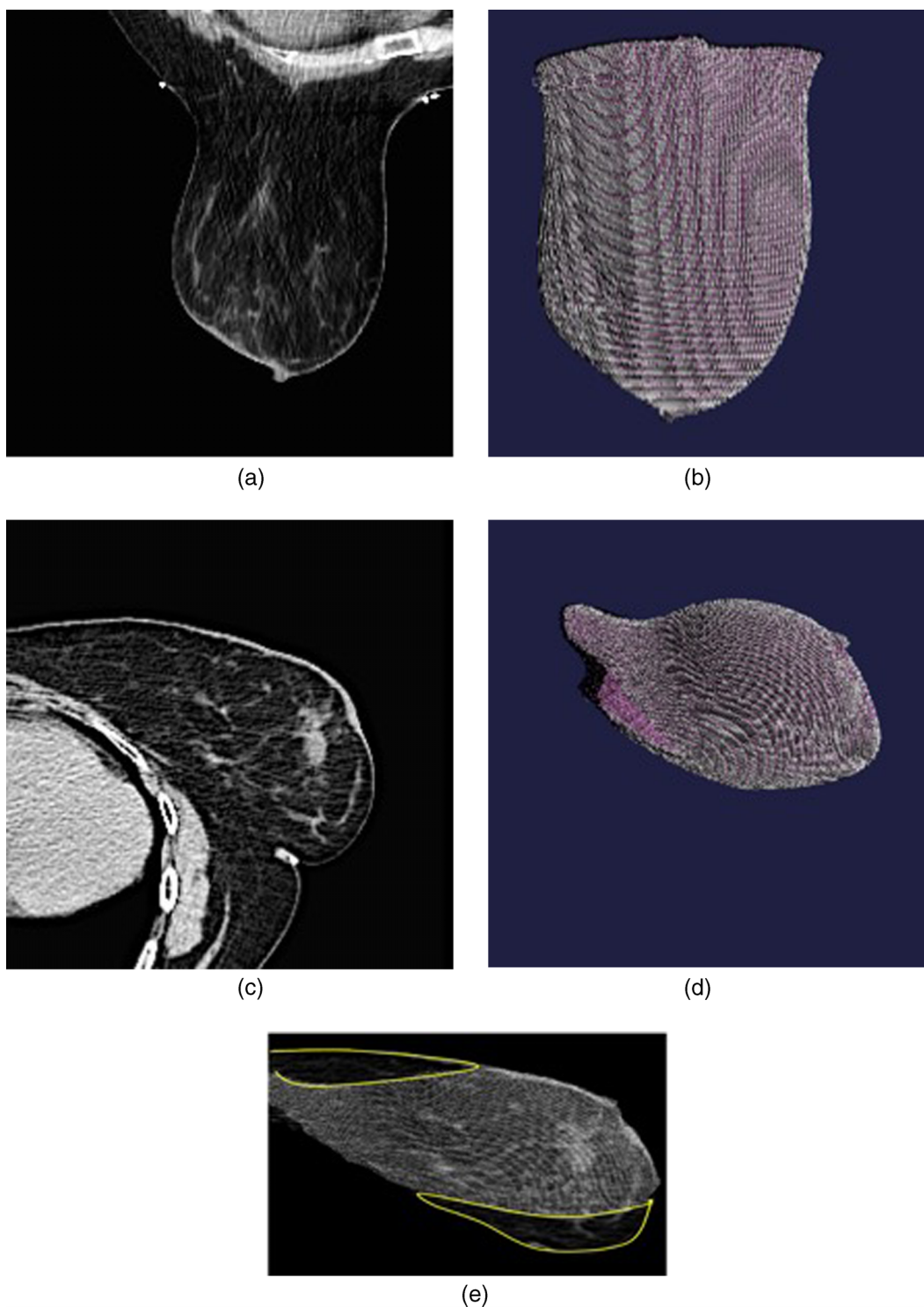
FIG. 5. Prone DICOM CT (a) and biomechanically simulated (b) data. Supine DICOM CT (c) and biomechanically simulated (d) data. The biomechanical simulation shown in (b) and (d) was generated from the DICOM CT images which had a resolution of 134×144. (c) and (d) were overlaid in (e) to give a direct comparison of our simulation to the DICOM CT (see color online version).

further breakdown of these results in terms of image resolution along with the average time.

Average time decreased appreciably, especially for the higher resolution hemisphere with 128 voxel diameter where the average time decreased by about 30 min. Overall, both accuracy and computation time improved notably between simulations run with the homogeneous initial guess and the

a priori initial guess, which is also illustrated in Fig. 7 for a random selection of ground-truth distributions. Figure 8 shows volume renderings of the ground-truth elasticity distribution (a), the resultant elasticity distribution when no *a priori* information was considered (b), and the resultant elasticity distribution when *a priori* information was used to form an initial guess (c) for a large IDC in quadrant I. Visually, it can

TABLE II. Overall results and results for simulations run with and without *a priori* information, with and without the FSA algorithm, and with lower and higher resolutions.

Overall results	Elasticity window		Displacement error
	±1 kPa (%)	±5 kPa (%)	<1 mm (%)
	87.60 ± 3.18	97.15 ± 4.73	96.81 ± 3.62
Averages	±1 kPa (%)	±5 kPa (%)	<1 mm (%)
Mean of datasets without *a priori*	87.60 ± 4.42	97.15 ± 1.26	96.81 ± 3.62
Mean of datasets with *a priori*	90.57 ± 3.23	98.15 ± 2.52	98.26 ± 2.82
Averages	±1 kPa (%)	±5 kPa (%)	<1 mm (%)
Mean of datasets without FSA	96.57 ± 2.38	98.75 ± 0.78	98.78 ± 1.01
Mean of datasets with FSA	96.40 ± 1.14	97.88 ± 1.31	97.48 ± 1.72
Averages	±1 kPa (%)	±5 kPa (%)	<1 mm (%)
Mean of datasets with lower resolution	92.02 ± 3.48	96.92 ± 1.32	98.87 ± 0.65
Mean of datasets with higher resolution	86.15 ± 4.10	98.38 ± 2.41	96.19 ± 1.87

be seen that Fig. 8(c) more closely matches the ground-truth distribution, without the distortion along the chest-wall and boundary distortions seen in Fig. 8(b). When the *a priori* information was not utilized, as in Fig. 8(b), the magnitude discrepancies and edge distortions are clear, which both agrees with, and thus strengthens, our numerical results. Table V shows excerpts of the individual results for a large IDC in quadrant II, a small fibroid in quadrant I, and a medium DCIS in quadrant III.

These results are selected to illustrate that regardless of tumor type, location, or size, the addition of *a priori* information significantly improves the results. This is further illustrated when considering the statistical significance of the average accuracy values. When *a priori* information was used to form an initial guess, the average displacement accuracy for the lower and higher resolution hemispheres increased, respectively, from 94.94% and 98.67% to 97.44% and 99.07%. A two-sample *t*-test between 20 different distributions confirmed that the improvements resulting from the use of *a priori* information were significant ($P < 0.05$). These results suggest that taking advantage of *a priori* HU data obtained from the clinical CT scans can reduce the convergence time of our simulation while improving the accuracy of the resulting elastic distribution.

3.C. Fast-simulated annealing

For ground-truth displacement distributions, the ground-truth elasticity distribution was prescribed as described in Sec. 2.C.1, and the ground-truth iteration number was set to 4000 iteration steps to allow the breast simulation adequate time to deform. The ground-truth iteration number was set to 4000 to allow the breast simulation adequate time to deform. The deformation of the particles was recorded for multiple iteration numbers, and at an iteration number of 4000, the maximum deformation increased by less than 0.01 mm, or 1% of our convergence criteria, indicating that the simulation had reached a state of equilibrium within 4000 iteration steps.

The FSA algorithm returned an average iteration number value of 2960 ± 590 iteration steps. The small discrepancy between this result and the ground-truth iteration number occurs because the combination of iterative binary search and the FSA algorithm allows for multiple solutions. More relevant is the resulting displacement and elasticity accuracy for the simulation run both with and without the FSA algorithm. Table II lists the resulting estimations of average elasticity and displacement accuracy for the distributions computed both with and without the FSA algorithm. The submillimeter convergence percentage of each instance (i.e.,

TABLE III. Example 64 and 128 voxel (lower and higher resolutions) test cases for a large fibroid in the center of the hemisphere, a small IDC in quadrant II, and a medium DCIS in quadrant IV.

| Large fibroid center	Elasticity window		Displacement error	
	±1 kPa (%)	±5 kPa (%)	<1 mm (%)	<3 mm (%)
Lower resolution	88.25	96.36	94.98	100.00
Higher resolution	80.42	98.45	89.95	100.00
Small IDC quadrant II	±1 kPa (%)	±5 kPa (%)	<1 mm (%)	<3 mm (%)
Lower resolution	85.28	98.85	96.58	100.00
Higher resolution	86.91	98.12	94.92	100.00
Medium DCIS quadrant IV	±1 kPa (%)	±5 kPa (%)	<1 mm (%)	<3 mm (%)
Lower resolution	74.86	99.31	99.83	100.00
Higher resolution	75.89	99.22	99.19	100.00
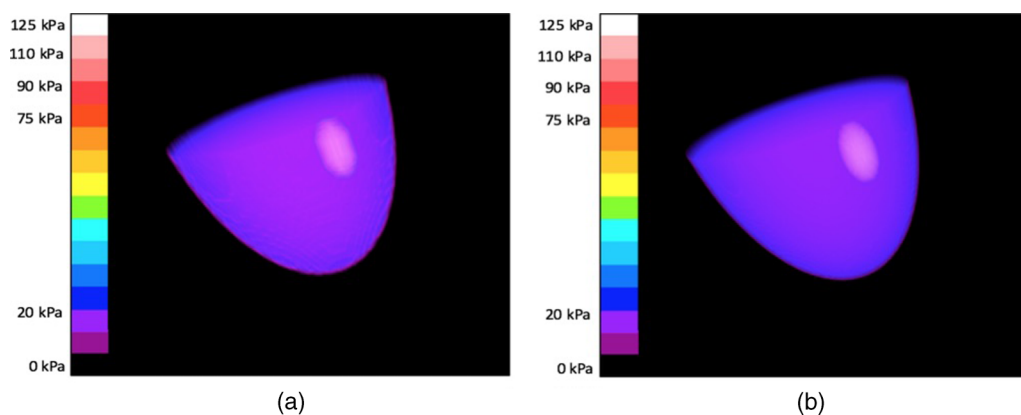
FIG. 6. Volume rendered comparison of a medium IDC in quadrant II within the (a) lower and (b) higher resolution hemispheres.

with and without FSA) was observed to be 97.45% and 98.78%, respectively. A two-sample *t*-test of 20 different distributions indicated that the difference between the mean values of each population was not significant ($P > 0.05$); therefore, use of the FSA algorithm allowed the iterative estimation process to converge correctly without reducing the integrity of the results. Figure 9 shows volume rendered elasticity distributions of the ground-truth (a) and estimated distributions with and without use of the FSA algorithm for a large IDC located in the center of the hemisphere [(b) and (c)]. It can be seen that both instances [(b) and (c)] result in a very similar volume rendering, where the location of the IDC is located accurately with some small discrepancies around the boundary of the tumor. From the numerical and visual results, we can conclude that use of the FSA algorithm allows our simulation to converge correctly. This will allow for us to more easily transition to clinical data—we will not have any preconceived notions of iteration number, yet we can still expect our simulation to determine accurate results. Comparing Figs. 8(b) and 9(b), it can be seen that elasticity was reconstructed with similar discrepancies in each case, indicating that tumor location does not obstruct our elasticity reconstruction. The use of *a priori* information, however, greatly impacted the resultant distribution, as shown in Fig. 8(c). A minor fact to note is that Fig. 9(a) is also much "brighter" than Fig. 8(a)—because the tumor was located in the center instead of the upper back quadrant, the window/level of the volume reconstruction did not have to be changed in order to see it.

Overall, our simulation converged with about 97% submillimeter accuracy. Though the errors were minimal, the largest elastic moduli discrepancies were seen around the boundary of the simulated tumors, and the largest displacement errors were seen both around the boundary of the tumor and the edge of the hemisphere. The use of *a priori* information greatly improved our results, while both use of the FSA algorithm and image resolution size do not affect the accuracy of our results. Tumor location also does not affect the accuracy of our outcome. The implications of these results are further discussed in Sec. 4.

4. DISCUSSION

In this work, a methodology for performing breast elasticity estimation using deformation resulting from the transition between supine and prone patient postures was presented. The procedure was developed and systematically assessed using a biomechanical simulation representing a breast in the prone position with a spherical tumor located within the breast. In order to investigate the accuracy and robustness of the approach for any given scenario, the synthetic tumors were given elasticity values from the literature used to represent three different common breast tumors: ductal carcinoma's *in situ*, invasive ductal carcinomas, and fibroadenomas and were positioned with different sizes throughout the breast tissue.

The biomechanical breast simulation was based on a physics-based approach. This choice was motivated by the previously shown accuracy of the approach for head and neck applications that were readily transferrable to the breast.[5] In addition, this model was validated for simulating motion caused by gravity, and the supine-to-prone deformation is known to be gravity-induced.[5,23,24] The implementation of this

TABLE IV. Table showing average values for low (64 voxel diameter) and high (128 voxel diameter) resolution hemispheres, both with and without *a priori* information.

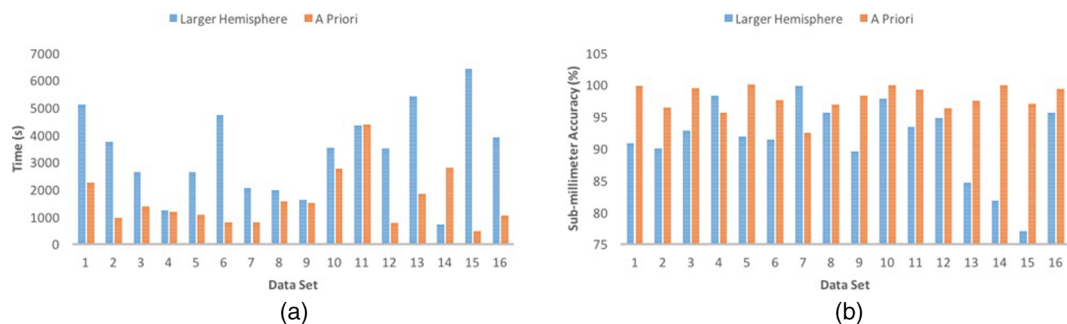| Hemisphere size	Elasticity window		Displacement error	
Averages	±1 kPa (%)	±5 kPa (%)	<1 mm (%)	Average time (s)
64 voxel mean	89.76 ± 1.12	96.40 ± 4.73	98.67 ± 3.62	272.50 ± 236.12
64 voxel with *a priori* mean	94.27 ± 6.38	97.43 ± 3.37	99.07 ± 1.08	218.06 ± 216.17
128 voxel mean	85.43 ± 4.37	97.89 ± 2.33	94.94 ± 4.09	3345.38 ± 1618.00
128 voxel with *a priori* mean	86.87 ± 3.23	98.87 ± 2.52	97.44 ± 2.17	1595.69 ± 1012.2

Fig. 7. (a) shows a time comparison for distributions with and without *a priori* information for random distributions, while (b) shows an accuracy comparison for the same datasets.

approach in a GPU environment enabled a high-resolution biomechanical simulation in nearly real-time. Inversing the forward deformation model allowed us to obtain elasticity maps for patient-specific biomechanical models that will be useful for reducing positioning errors in adaptive radiotherapy. Using the well-validated constitutive model previously used for head and neck allowed us to purely focus on the accuracy and feasibility of the inverse analysis, rather than the model's accuracy in regards to simulating gravity-induced deformations. While the usage of such a GPU-based, biomechanical model has been recently validated for head and neck tissues, future studies will focus on the usage of such a model for breast tissue, which needs to be clinically validated using an extensive patient study. Model errors in such studies typically stem either from tissue elasticity estimation errors or from the model's inability to represent the complex anatomical deformation. Having shown in this paper that the tissue elasticity estimation errors will be minimal for this biomechanical model, future work will focus on a clinical study to enumerate the model's ability to quantitatively represent the anatomy.

While most deformable modeling efforts may be insensitive to soft-tissue elasticity data, our approach has a direct relationship with the properties of soft tissue since it relies on the supine-to-prone breast deformation, which is driven by gravity. The ground-truth displacements required for our methodology depend on the ability to register prone and supine breast images with a one-to-one correspondence.

Due to the large deformation induced to the breast tissue, image registration between these postures is a challenging problem. Various deformable image registration algorithms have been investigated by peers specifically for the prone-to-supine breast transition.[24,33,34] Future work will focus on further investigating a deformable image registration technique that provides accurate ground-truth data and a one-to-one correspondence between breast tissue in the prone and supine positions.

In our approach, we have employed a linear elastic deformation model to deform the breast anatomy from supine to prone patient posture. Such a deformation may be large enough to cite a need for hyperelastic model to represent the tissue behavior. Our future work will focus on extending the method to a hyperelastic regime. Such an analysis will require more patient postures to be imaged.

The iterative binary search optimization algorithm, along with the FSA algorithm, allowed for the estimation of elastic properties for the biomechanical model based upon the deformation of each mass element. The performance of the algorithm was confirmed with the high elasticity and displacement accuracy that was achieved. The iterative optimization algorithm allowed each mass element to converge individually, so that even tumors with diameters as small as 5 mm were located accurately. While our simulation study used a simplified framework that modeled tumors spherically, the per voxel approach of our inverse analysis should allow sufficient delineation of irregular tumors shapes as well. We
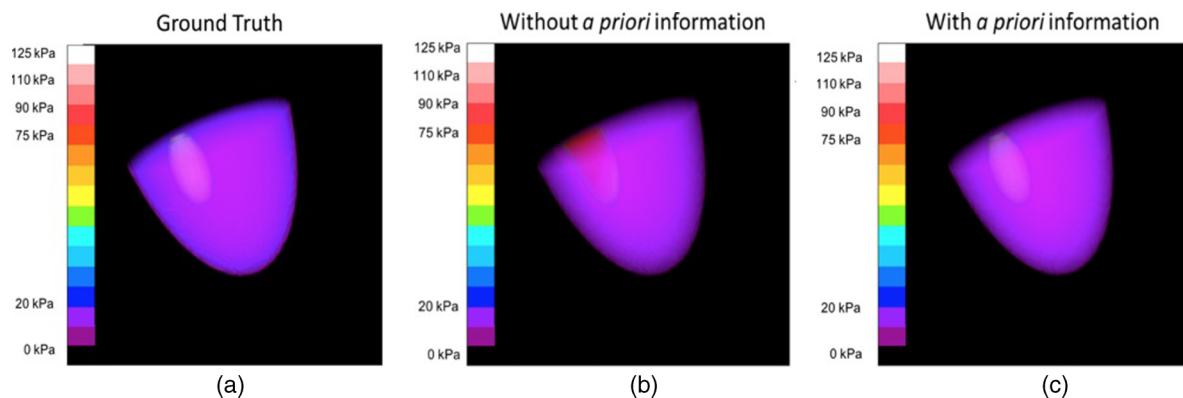

Fig. 8. Volume renderings of small IDC located in quadrant II. (a) shows the ground-truth distribution, (b) shows the reconstruction with a random initial guess, and (c) shows the reconstruction using *a priori* information to make an informed initial guess.

TABLE V. Example of individual cases with and without *a priori* information for a large IDC in quadrant II, a small fibroid in quadrant I, and a medium DCIS in quadrant III.

	Elasticity window		Displacement error	
Large IDC quadrant II	±1 kPa (%)	±5 kPa (%)	<1 mm (%)	<3 mm (%)
Without *a priori*	86.43	97.68	88.30	100.00
With *a priori*	96.90	98.25	100.00	100.00
Small fibroid quadrant I	±1 kPa (%)	±5 kPa (%)	<1 mm (%)	<3 mm (%)
Without *a priori*	72.20	99.62	90.02	100.00
With *a priori*	81.24	99.64	96.47	100.00
Medium DCIS quadrant III	±1 kPa (%)	±5 kPa (%)	<1 mm (%)	<3 mm (%)
Without *a priori*	80.86	92.29	68.38	100.00
With *a priori*	91.20	99.03	95.49	100.00

believe the algorithm has potential to recognize other items of interest that may be located within the breast that were not investigated here. Future work will investigate the accuracy of our approach for irregular tumor shapes and sizes, as well as for irregular breast shapes.

Our results showed that an accuracy of 98% was achieved in estimating the ground-truth elasticity. Because of the per voxel nature of our approach, variations in the size of the tumor and the breast geometry had negligible impact on the accuracy of the estimation process. Our analysis indicated that the elasticity can be successfully reconstructed for tumors with a diameter as small as 5 mm and as large as 1.5 cm within the breast tissue. Changes in image resolution and geometry size showed no significant impact on the resulting accuracy, indicating that the CT image resolution should not influence the resulting elasticity estimation. The geometry size alternatives also indicated that the biomechanical simulation successfully represented different breast sizes.

The elasticity information that we obtain through this methodology will be used to design a new immobilization device specifically for precise and reproducible breast positioning. Ideal breast geometry for radiotherapy is similar to that achieved in the prone orientation, without the discomfort and associated normal tissue doses.[35] With the robotic assistance of an immobilization device, this ideal position can be achieved in a more comfortable, supine orientation. Our high-resolution, physics-based breast model will act as a control module for such a robotic system, simulating patient-specific breast geometry and its deformation when interacting with the robotic system.[3] Future work will focus on improving the breast simulation to more realistically simulate the breast anatomy, eventually progressing to patient data. We believe this methodology can also be readily transitioned to other anatomies such as the lung, liver, and head and neck for radiotherapy applications.

Because of the imaging techniques within current radiotherapy workflows, our current methodology uses DICOM CT images to construct the biomechanical model. Future work will focus on expanding this methodology to be coupled with US and MR measurements to further improve the model-guided elasticity estimation process. Evolutionary algorithms will be investigated and their functionality compared to that of the FSA and binary search algorithms. The linear elasticity assumptions will be expanded into a hyperelastic regime in order to more accurately depict the biological tissue. Finally, the biomechanical simulation will be implemented on a multi-GPU platform to increase the resolution of the model and decrease the computation time. These efforts are crucial in order to apply the methodology in clinical radiotherapy practice.
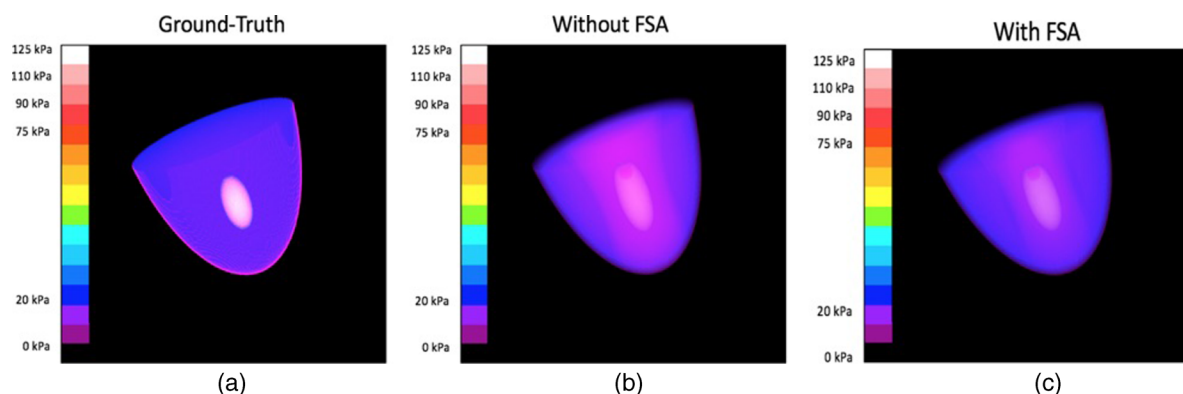

FIG. 9. Volume rendering of a large IDC located in the center of hemisphere. (a) shows the ground-truth distribution, (b) shows the reconstruction without the use of the FSA algorithm, and (c) shows the reconstruction using the FSA algorithm.

5. CONCLUSIONS

In this paper, we present a systematic study of a novel GPU-based inverse analysis methodology for breast tissues using supine/prone CT image datasets. The methodology was investigated using a forward model, GPU-based, physics-based breast simulation that was iteratively deformed to represent the deformation of the breast between supine and prone orientations. The inverse analysis consisted of a gradient-based binary search optimization scheme that, coupled with a fast-simulated annealing algorithm, updated the spatial elasticity distribution of the breast tissue. Our analysis showed that the methodology enables a 97% accuracy in elasticity estimation of homogeneous breast tissue and an embedded tumor with regards to our novel error metric only using the two postures. These results indicate that our methodology has the potential to be readily applied with great accuracy to advance breast positioning techniques in clinical radiotherapy practice.

ACKNOWLEDGMENTS

NOMENCLATURE

a	Mass element
b	Connected element
$\vec{f}_{Y,ab}$	Tensile force on element a from connected element b
$\vec{f}_{S,ab}$	Shear force on element a from connected element b
$\vec{f}_{v,ab}$	Dashpot damping force on element a from connected element b
$\vec{f}_a$	Internal corrective force on element a
$\vec{v}_a^{n+1}$	Velocity of mass element a at iteration $n+1$
$\vec{x}_a^{n+1}$	Position of mass element a at iteration $n+1$
δ	Time step between iterations
m_a	Mass of mass element a
$\vec{g}$	Acceleration due to gravity
$F_{E,a}$	Elastic force on mass element a
$E[i]$	Elastic modulus of voxel i
$d[i]$	Displacement of voxel i
L	Inter element distance before deformation

[a] Electronic mail: khasse@mednet.ucla.edu
[b] Electronic mail: jneylon@mednet.ucla.edu
[c] Electronic mail: ksheng@mednet.ucla.edu
[d] Electronic mail: ASanthanam@mednet.ucla.edu

[1] A. C. Society, Breast Cancer Key Statistics, 2015, available at http://www.cancer.org/cancer/breastcancer/detailedguide/breast-cancer-key-statistics.

[2] T. Fatunase, Z. Wang, S. Yoo, J. L. Hubbs, R. G. Prosnitz, F. F. Yin, and L. B. Marks, "Assessment of the residual error in soft tissue setup in patients undergoing partial breast irradiation: Results of a prospective study using cone-beam computed tomography," Int. J. Radiat. Oncol., Biol., Phys. **70**(4), 1025–1034 (2008).

[3] J. Neylon, K. Hasse, and A. Santhanam, "Modeling and simulation of tumor-influenced high resolution real-time physics-based breast models for model-guided robotic interventions," Proc. SPIE (unpublished).

[4] W. Maurel, *Biomechanical Models for Soft Tissue Simulation*, ESPRIT Basic Research Series (Springer-Verlag, Berlin, New York, NY, 1998), Vol. XVIII, p. 173.

[5] J. Neylon, X. Qi, K. Sheng, R. Staton, J. Pukala, R. Manon, D. A. Low, P. Kupelian, and A. Santhanam, "A GPU based high-resolution multilevel biomechanical head and neck model for validating deformable image registration," Med. Phys. **42**(1), 232–243 (2015).

[6] C. P. South, M. Partridge, and P. M. Evans, "A theoretical framework for prescribing radiotherapy dose distributions using patient-specific biological information," Med. Phys. **35**, 4599–4611 (2008).

[7] B. Titz and R. Jeraj, "An imaging-based tumour growth and treatment response model: Investigating the effect of tumour oxygenation on radiation therapy response," Phys. Med. Biol. **53**, 4471–4488 (2008).

[8] D. Fuentes *et al.*, "Computational modeling and real-time control of patient-specific laser treatment of cancer," Ann. Biomed. Eng. **37**, 763–782 (2009).

[9] O. Chilali, A. Ouzzane, M. Diaf, and N. Betrouni, "A survey of prostate modeling for image analysis," Comput. Biol. Med. **53**, 190–202 (2014).

[10] T. A. Krouskop, T. M. Wheeler, F. Kallel, B. S. Garra, and T. Hall, "Elastic moduli of breast and prostate tissues under compression," Ultrason. Imaging **20**(4), 260–274 (1998).

[11] Z. L. Wang, L. Sun, Y. Li, and N. Li, "Relationship between elasticity and collagen fiber content in breast disease: A preliminary report," Ultrasonics **57**, 44–49 (2015).

[12] B. S. Garra, E. I. Cespedes, J. Ophir, S. R. Spratt, R. A. Zuurbier, C. M. Magnant, and M. F. Pennanen, "Elastography of breast lesions: Initial clinical results," Radiology **202**(1), 79–86 (1997).

[13] A. Goddi, M. Bonardi, and S. Alessi, "Breast elastography: A literature review," J. Ultrasound **15**(3), 192–198 (2012).

[14] H. Rivaz, P. Foroughi, I. Fleming, R. Zellars, E. Boctor, and G. Hager, "Tracked regularized ultrasound elastography for targeting breast radiotherapy," Med. Image Comput. Comput. Assisted Intervention **12**(Pt. 1), 507–515 (2009).

[15] A. Evans, P. Whelehan, K. Thomson, D. McLean, K. Brauer, C. Purdie, L. Jordan, L. Baker, and A. Thompson, "Quantitative shear wave ultrasound elastography: Initial experience in solid breast masses," Breast Cancer Res. **12**(6), R104 (2010).

[16] M. M. Doyley, "Model-based elastography: A survey of approaches to the inverse elasticity problem," Phys. Med. Biol. **57**(3), R35–R73 (2012).

[17] K. M. Hiltawsky, M. Kruger, C. Starke, L. Heuser, H. Ermert, and A. Jensen, "Freehand ultrasound elastography of breast lesions: Clinical results," Ultrasound Med. Biol. **27**(11), 1461–1469 (2001).

[18] H. T. Liu, L. Z. Sun, G. Wang, and M. W. Vannier, "Analytic modeling of breast elastography," Med. Phys. **30**(9), 2340–2349 (2003).

[19] A. Itoh, E. Ueno, E. Tohno, H. Kamma, H. Takahashi, T. Shiina, M. Yamakawa, and T. Matsumura, "Breast disease: Clinical application of US elastography for diagnosis," Radiology **239**(2), 341–350 (2006).

[20] A. M. Kirby, P. M. Evans, E. M. Donovan, H. M. Convery, J. S. Haviland, and J. R. Yarnold, "Prone versus supine positioning for whole and partial-breast radiotherapy: A comparison of non-target tissue dosimetry," Radiother. Oncol. **96**(2), 178–184 (2010).

[21] M. Lu, H. Zhang, J. Wang, J. Yuan, Z. Hu, and H. Liu, "Reconstruction of elasticity: A stochastic model-based approach in ultrasound elastography," Biomed. Eng. Online **12**, Article No. 79 (2013).

[22] M. M. Doyley, S. Srinivasan, S. A. Pendergrass, Z. Wu, and J. Ophir, "Comparative evaluation of strain-based and model-based modulus elastography," Ultrasound Med. Biol. **31**(6), 787–802 (2005).

[23] V. Rajagopal, A. Lee, J. H. Chung, R. Warren, R. P. Highnam, P. M. Nielsen, and M. P. Nash, "Towards tracking breast cancer across medical images using subject-specific biomechanical models," Med. Image Comput. Comput. Assisted Intervention **10**(Pt. 1), 651–658 (2007).

[24] L. Han, J. H. Hipwell, B. Eiben, D. Barratt, M. Modat, S. Ourselin, and D. J. Hawkes, "A nonlinear biomechanical model based registration method for aligning prone and supine MR breast images," IEEE Trans. Med. Imaging **33**(3), 682–694 (2014).

[25]M. M. Doyley, P. M. Meaney, and J. C. Bamber, "Evaluation of an iterative reconstruction method for quantitative elastography," Phys. Med. Biol. **45**(6), 1521–1540 (2000).

[26]F. Kallel and M. Bertrand, "Tissue elasticity reconstruction using linear perturbation method," IEEE Trans. Med. Imaging **15**(3), 299–313 (1996).

[27]P. E. Gill, W. Murray, and M. H. Wright, *Practical Optimization* (Academic, London, New York, 1981), Vol. XVI, p. 401.

[28]D. Fu, S. F. Levinson, S. M. Gracewski, and K. J. Parker, "Non-invasive quantitative reconstruction of tissue elasticity using an iterative forward approach," Phys. Med. Biol. **45**(6), 1495–1509 (2000).

[29]H. Zhi, X. Y. Xiao, H. Y. Yang, Y. L. Wen, B. Ou, B. M. Luo, and B. L. Liang, "Semi-quantitating stiffness of breast solid lesions in ultrasonic elastography," Acad. Radiol. **15**(11), 1347–1353 (2008).

[30]S. N. Bhatti and M. Sridhar-Keralapura, "A novel breast software phantom for biomechanical modeling of elastography," Med. Phys. **39**(4), 1748–1768 (2012).

[31]M. Urata, Y. Kijima, M. Hirata, Y. Shinden, H. Arima, A. Nakajo, C. Koriyama, T. Arigami, Y. Uenosono, H. Okumura, K. Maemura, S. Ishigami, H. Yoshinaka, and S. Natsugoe, "Computed tomography Hounsfield units can predict breast cancer metastasis to axillary lymph nodes," BMC Cancer **14**, Article No. 730 (2014).

[32]W. Assaad and S. Misra, "Combining ultrasound-based elasticity estimation and FE models to predict 3D target displacement," Med. Eng. Phys. **35**(4), 549–554 (2013).

[33]B. Eiben, V. Vavourakis, J. H. Hipwell, S. Kabus, T. Buelow, C. Lorenz, T. Mertzanidou, S. Reis, N. R. Williams, M. Keshtgar, and D. J. Hawkes, "Symmetric biomechanically guided prone-to-supine breast image registration," Ann. Biomed. Eng. **44**(1), 154–173 (2015).

[34]K. Dowlatshahi, R. Alvarado, and K. Kopckash, "The role of image-guided surgery in breast cancer," Image-Guided Cancer Therapy 877–890 (2013).

[35]S. C. Formenti, J. Keith Dewyngaert, G. Jozsef, and J. D. Goldberg, "Prone vs supine positioning for breast cancer radiotherapy," JAMA **308**(9), Article No. 861 (2012).